Precision Engineering 93 (2025) 515–527

Contents lists available at ScienceDirect

Precision Engineering

journal homepage: www.elsevier.com/locate/precision

Time delay compensation in high-speed diamond turning of freeform surface using independent fast tool servo with a long stroke

Takeshi Hashimoto, Jiwang Yan *

Department of Mechanical Engineering, Faculty of Science and Technology, Keio University, 3-14-1 Hiyoshi, Kohoku-ku, Yokohama, 223-8522, Japan

ARTICLE INFO

Handling editor: R. Leach

Keywords:
Freeform surface fabrication
Diamond turning
Fast tool servo
Time delay
On-machine evaluation

ABSTRACT

The demand for wearable device applications has continuously grown in recent years, especially with the significant rise of augmented and virtual reality technologies. Freeform optics plays a crucial role in these devices by enhancing optical performance, shortening the light path, and reducing the weight, all while allowing for smaller, lighter systems with higher efficiency. The independent fast tool servo (FTS)-based diamond-turning method stands out as a highly effective technique for fabricating freeform shapes with high accuracy and productivity. However, microsecond-order time delays occur within the system, significantly impacting form accuracy as machining speeds increase. This study explores the sources of form errors in freeform surface fabrication associated with the FTS diamond-turning process, with particular attention to the effects of clocking angle errors caused by the time delay. These errors were found to greatly affect form accuracy, especially at higher machining speeds. The FTS position data were analyzed, and time delays under various operational conditions due to servo control were confirmed. To precisely identify the extent of the time delay, a cylindrical surface was machined under high-speed conditions, and the clocking angle error was measured using a non-contact chromatic probe. Results showed that time delays originating from the machine platform had a significant effect on form accuracy. By accurately identifying and compensating for these time delays, the clocking angle error was eliminated. To validate the effectiveness of the time-delay compensation strategy, a cylindrical freeform surface was machined after the compensation, and the clocking angle error was minimized down to 0.00014° evaluated by on-machine measurement. The form accuracy of the freeform machining result after compensation was achieved at 0.85 μm PV. This study establishes a methodology for identifying and compensating for time delays in an independent FTS system, contributing to improved form accuracy in freeform optics fabrication.

1. Introduction

In recent years, technologies utilizing advanced optical components have rapidly developed across various fields, from space applications to devices that support daily life. These optical components are driven by the technical requirements of each product, such as telescopes for space observation [1,2], light detection and ranging (LiDAR) devices for autonomous vehicles and fast-moving drones [3,4], and augmented reality (AR) and virtual reality (VR) applications. These applications typically demand high-resolution imaging quality with an effective light path for imaging devices, detection of specific wavelengths using unique optical materials for sensing devices, and lightweight components for wearable devices. In particular, for AR/VR applications, because headsets still maintain a box-like form factor, pancake optics designs and polarization-based optical folding have been developed to reduce the size of near-eye displays, while various combiner optics designs aid in achieving smaller form factors [5,6]. To meet the stringent demands for size and performance, complex surface designs are increasingly used to reduce the light path and correct astigmatism in optical devices, enhancing performance [7,8].

Freeform optics offer exceptional optical efficiency and reduce the need for multiple optical elements due to their flexible shape design. Freeform surface designs provide significant advantages over conventional optics, enabling more compact and simplified systems, expanding the field of view, and improving image resolution [9,10]. These designs often involve complex surfaces described by equations such as the Alvarez lens, which adjusts focal length through transverse shifts of two surfaces and is expressed by XY-polynomials [11,12], and the Zernike

* Corresponding author.
E-mail address: yan@mech.keio.ac.jp (J. Yan).

https://doi.org/10.1016/j.precisioneng.2025.02.006
Received 22 October 2024; Received in revised form 25 January 2025; Accepted 3 February 2025
Available online 6 February 2025
0141-6359/© 2025 The Authors. Published by Elsevier Inc. This is an open access article under the CC BY license (http://creativecommons.org/licenses/by/4.0/).

Downloaded from Yan Laboratory, Keio University at http://www.yan.mech.keio.ac.jp. Redistribution is subject to copyright licence from the journal publisher.

polynomial for describing wavefront aberrations [13,14], to control light paths and wavefronts more precisely and efficiently. Such innovations have led to the increased integration of freeform optics into head-mounted displays (HMDs) for VR and AR applications [15,16].

Ultra-precision diamond turning is a well-established process for fabricating high-precision optical components, particularly rotationally symmetric ones such as spherical or aspherical optics. In recent years, this process has expanded through the introduction of C-axis control in the work-holding spindle. Synchronization between the C-axis and other linear axes has enabled the fabrication of non-rotationally symmetric surfaces, including complex freeform shapes and lens arrays, using a method known as slow-tool servo (STS) diamond turning [17]. Freeform surface fabrication with STS diamond turning has demonstrated form error compensation, achieving errors of less than 1 μm [18,19]. For example, Nagayama et al. used STS diamond turning to fabricate microstructures on single-crystal silicon with nanometer-scale accuracy [20]. However, despite its high accuracy, the machining speed remains insufficient for meeting high-productivity demands seen with axis-symmetric components. In contrast, fast-tool servo (FTS) diamond turning uses a specially equipped control axis capable of high-frequency movement. FTS systems are typically driven by piezo actuators, voice coil motors, or Maxwell's electromagnetic force methods. FTS is widely used for fabricating surface structures such as microprisms, lens arrays, toroids, and off-axis aspherics with small sagittas [17]. The mechanical stroke limitation of conventional FTS, driven by piezoelectric materials, is commercially available up to 100 μm, which restricts its application in producing high-precision freeform optics with millimeter-scale sagitta.

Recently, a new type of long-stroke FTS, driven by a voice coil motor and high-frequency servo control technology with high-resolution positioning, has become commercially available [21]. This FTS system allows for the fabrication of a wide range of designs, from micrometer-scale structures to millimeter-scale sagittal freeform surfaces, including sine waves, dual sinusoidal patterns, and large freeform shapes, with increased productivity [22–24]. One of the key limitations in FTS control is the signal processing speed capability of the CNC controller, particularly in high-speed operations, which is critical for ensuring optimal surface quality. To achieve this, the command generation rate for the FTS should be at least 20 times higher than the frequency response of the positioning system [25]. Therefore, a piezoelectric-driven FTS or voice-coil motor-driven FTS is controlled by an independent control system that is separate from the base machine controller to utilize the high-speed features of the FTS. However, despite the precise control in high-speed reciprocation of the FTS actuator, a certain amount of time delay exists within the system. From a control theory perspective, motion control systems typically experience a delay between the command signal and the actual motion. This time delay introduces a clocking angle error in the high-speed FTS diamond turning process, directly impacting the form accuracy of the optical component. The error becomes more significant as the surface slope increases or the spindle rotation speed rises. Therefore, to meet the recent demands for higher accuracy and productivity in freeform optics using the long-stroke FTS system, it is crucial to understand the system characteristics that contribute to clocking angle error.

Tanikawa et al. highlighted angular misalignment problems in the diamond-turning process using independent FTS [26]. They proposed a calibration process for identifying time delays by machining dimples and measuring their locations to determine angular misalignment errors. However, the reasons for these time delays and related factors remain unclear, and system behavior regarding time delays has not yet been fully examined. Additionally, their experiments involved identifying time delays in FTS systems with micrometer-scale strokes. To fabricate freeform surfaces with millimeter- or 10-mm-scale sagitta with sufficient accuracy, time-delay identification under long-stroke conditions is necessary. Developing a strategy to correct clocking angle errors through time-delay identification and compensation in independently controlled FTS systems is crucial. This study investigates the form errors introduced by long-stroke FTS diamond turning, focusing specifically on the impact of time-delay-induced clocking angle errors. The influence of clocking angle errors on freeform surface fabrication was analyzed by simulating the machining of a cylindrical surface, revealing that clocking angle errors significantly affect form accuracy and is related to the signal processing delay, particularly in high-speed FTS diamond turning. Time delays in the FTS system were investigated by analyzing position data and decomposing the delay sources. The time delay caused by servo control under various operational conditions was examined. To precisely identify the time delay, a cylindrical surface was machined under high-speed conditions, and the clocking angle error was measured using a non-contact chromatic probe. It was found that time delays originating from the machine platform significantly affected form accuracy. The identified time delay was directly compensated for, and the clocking angle error in cylindrical surface fabrication was eliminated. Finally, using the identified time delay for compensation, high-speed machining of cylindrical freeform surfaces was demonstrated, where the residual clocking angle error was minimized. This study establishes a methodology for identifying and compensating for time delays in FTS systems, contributing to improved form accuracy in the high-speed production of freeform optics using independently controlled FTS systems.

2. Theoretical analysis on the impact of clocking angle error on form accuracy

To describe the positional deviation in the z-axis direction Δz, when a freeform surface is rotated by a clocking angle φ as illustrated in Fig. 1, we start with the equation in Cartesian coordinates, where the freeform surface shape is represented as $z = f(x,y)$ and the rotated freeform surface $z' = g(x, y)$. The deviation is given by Equation (1) and by mapping the displacement Δz in both circumferential and radial directions, the form error associated with the clocking angle error φ, which can be characterized,

$$\Delta z = z - z' = f(x,y) - g(x,y) \,. \tag{1}$$

In this context, we consider the local slope component in the circumferential direction. This local slope angle component, S_θ, represents the partial derivative with respect to θ around the θ axis of the freeform surface equation $z = f'(r,\theta)$, which is transformed into polar coordinates, as shown in Fig. 2, and is described as follows:

$$S_\theta = \frac{\partial f'}{\partial \theta} = \frac{\partial f}{\partial x}\cdot\frac{\partial x}{\partial \theta} + \frac{\partial f}{\partial y}\cdot\frac{\partial y}{\partial \theta} \,. \tag{2}$$

If a clocking angle error φ occurs in the fabricated shape, the

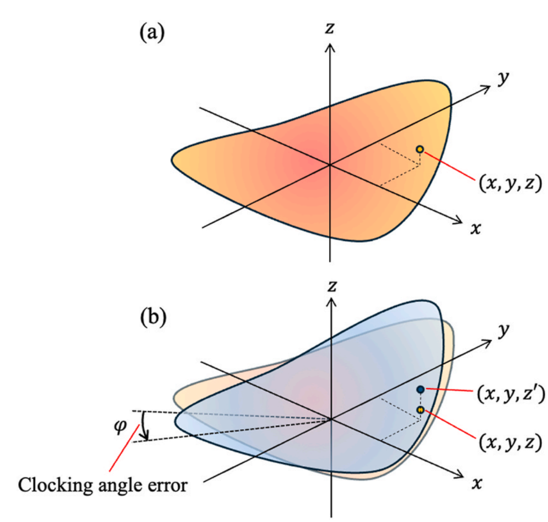

Fig. 1. Form error induced by clocking angle error on a freeform surface: (a) before rotation, (b) after rotation with a clocking angle error of φ.

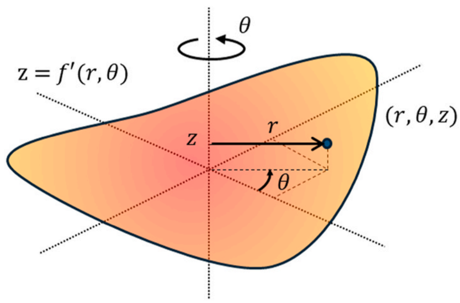

Fig. 2. Local slope calculation of the given surface converted to polar coordinate.

displacement in the Z-axis direction between the design value and the rotated value at any point on $z = f'(r,\theta)$ is expressed using the local slope angle component S_θ, and the clocking angle φ as follows:

$$\Delta z = \pi r \cdot \frac{\varphi}{180} \cdot S_\theta, \tag{3}$$

the maximum height at this location was determined by calculating the difference between the maximum and minimum values of Δz incorporating the radial distance r, which is from the rotational center of the sample surface to the point of interest, the clocking angle φ and the local slope angle S_θ. The absolute value of this maximum height indicates the form error Er resulting from the error in the clocking angle.

$$Er = |max(\Delta z) - min(\Delta z)|, \tag{4}$$

considering a cylinder with a diameter of 50 mm and a radius of curvature (ROC) of 100 mm, the local slope map in the concentric direction was calculated, as shown in Fig. 3. The calculation results of form errors caused by clocking angle errors of 0.001°, 0.01°, and 0.015° are shown in Fig. 4, illustrating how form errors increase as the clocking angle error rises. The relationship between the form error and clocking errors based on the radius of the cylinder surface is depicted in Fig. 5.

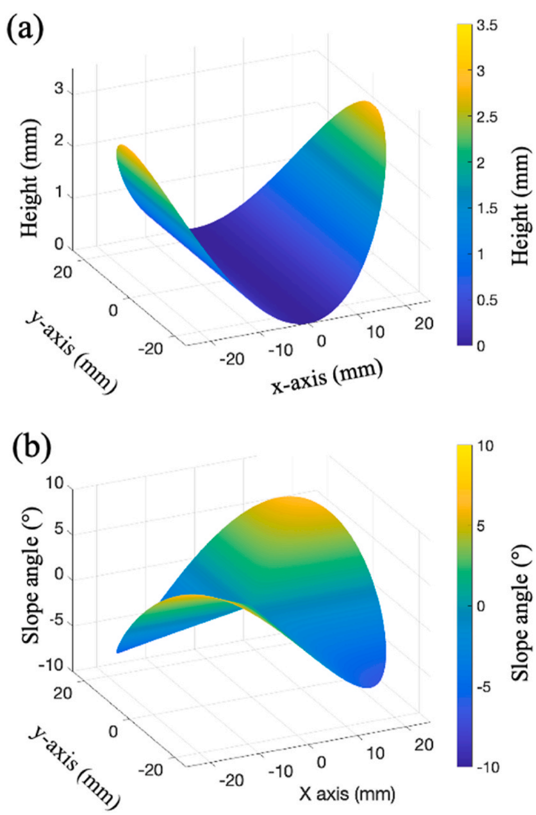

Fig. 3. Calculation result of local slope, 100 mm ROC cylinder surface with 50 mm diameter, (a) height distribution map, (b) local slope angle map.

According to repetitive control theory in servo control, time delays are unavoidable due to the time required for sensing and control signal transmission [27,28]. The relationship between the clocking angle error and time delay at a spindle rotational speed of 1000 rpm is shown in Fig. 5. The smaller ROC, the larger the slope angle in the circular direction, leading to a proportional increase in the clocking angle error. The clocking angle error originates from the time delay T_d in seconds, which can be derived using the rotational rate N in rpm and the clocking angle error φ in degrees. The cumulative rotation angle θ_N in a second from the spindle rotational speed of N is described in Equation (5). The unit of the θ_N is degrees per second. Therefore, to derive the time delay T_d using the spindle rotational speed and the clocking angle error, it can be described in Equation (6) as follows:

$$\theta_N = 360 \cdot (N / 60), \tag{5}$$

$$T_d = \varphi / \theta_N, \tag{6}$$

considering the relationship between the shape of a freeform surface and the required form accuracy, the acceptable value for the clocking angle error is determined using Equations (2) and (3). The time delay error is calculated based on the desired spindle rotation rate using Equation (6). For a form accuracy within 1 μm PV on a 100 mm ROC cylinder with a 50 mm diameter, for instance, the time delay from the control system needs to be within 1.67 μs or less. This shows that the clocking angle error, influenced by the time delay, has a significant impact on form accuracy in high-speed machining operations.

3. Experimental system

3.1. Machine tool and FTS system

An ultraprecision diamond-turning machine, Nanoform X (AMETEK Precitech Inc., USA), with XYZBC five-axis simultaneous control, was used as the ultraprecision platform in this study. The lathe features an air-bearing work spindle with high-resolution positioning control for the C-axis and oil hydrostatic linear stages for the X-, Y-, Z-, and B-axis rotary tables, all with full closed-loop feedback control for sub-nanometric feedback resolution. This machine employs an independent fast-tool servo (FTS5000, AMETEK Precitech Inc., USA) as an additional axis (W-axis), allowing synchronized position control, calculated based on the X- and C-axis encoder data. The independent FTS features an air-bearing piston with a 5 mm full stroke. Its position control utilizes a fully closed feedback system with a glass-scale linear encoder for nanometric feedback, driven by a voice coil motor for reciprocating motion, along with a counterbalance acting as a mass damper. This FTS system can achieve 2000 μ m amplitude sinusoidal motion at 100 Hz, with 40G peak acceleration and 25G continuous acceleration [21].

A non-contact chromatic confocal optical probe (CHRocodile 2 S, Precitec GmbH) was integrated with the machine to evaluate the machined surface as an on-machine metrology system. This probe offers nanometer-level axial resolution and a high-speed data collection capability of up to 10 kHz. The machine layout is shown in Fig. 6(a). The FTS, functioning as the W-axis, is positioned on the B-axis and aligned parallel to the Z-axis. A diamond tool is mounted on the tool snout at the actuator's nose. The optical probe is installed on the B-axis next to the FTS (W-axis) to measure the clocking angle error post-machining without removing the workpiece from the vacuum chuck. Fig. 6(b) shows the machine setup used for the experiment. The workpiece was placed on the C-axis spindle nose with a vacuum chuck and had a reference flat for alignment, which was set to the C-axis reference position of the diamond-turning machine and FTS.

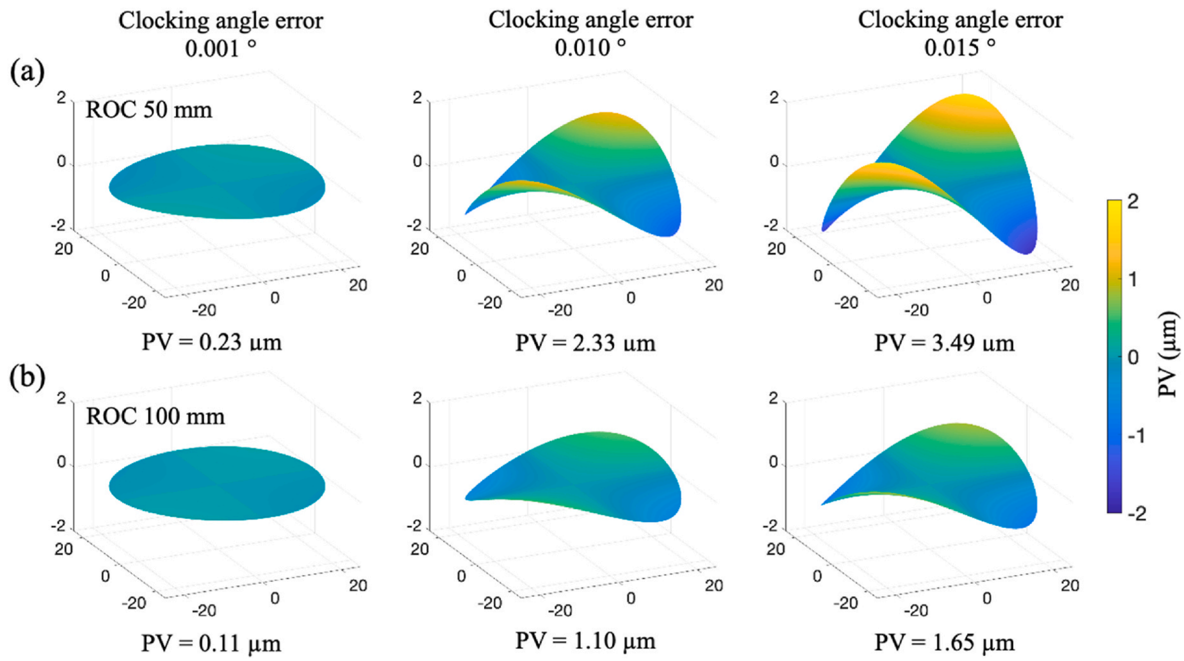

Fig. 4. Simulation results of form error due to variations in clocking angle error across two designs: (a) 50 mm ROC cylinders, (b) 100 mm ROC cylinders, respectively.

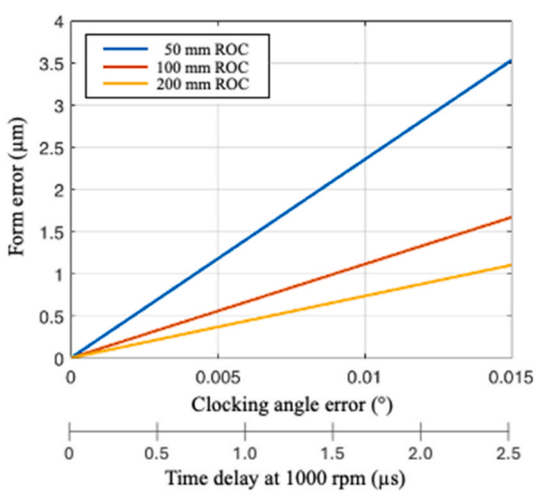

Fig. 5. Relationship of form error and clocking angle error (time delay amount at 1000 rpm spindle speed) and ROC cylinders, 50 mm diameter.

3.2. System signal flow

Fig. 7 shows an overall view of the signal flow in this system, including the FTS and the on-machine evaluation probe. The FTS system was connected to the machine platform by receiving the X- and C-axis encoder signals. These signals from the machine platform enter the FTS command generator to generate the W-axis command for controlling the actuator at the tool tip position. The signal from the optical probe for on-machine measurement is collected simultaneously with the machine-axis encoder information to describe the machined surface using the machine-axis coordinates as discrete data. Fig. 8 shows the signal flow inside the FTS system in detail. The X- and C-axis encoder signals are sent to the command generator from the base machine in the FTS system. Inside the command generator, the W-axis command position, based on the part program of the desired shape, was calculated and sent to the controller for W-axis control. The actual position of the W axis was monitored using a glass scale in the FTS actuator for position feedback control. The commands and actual position information were simultaneously acquired from the controller using a data analyzer.

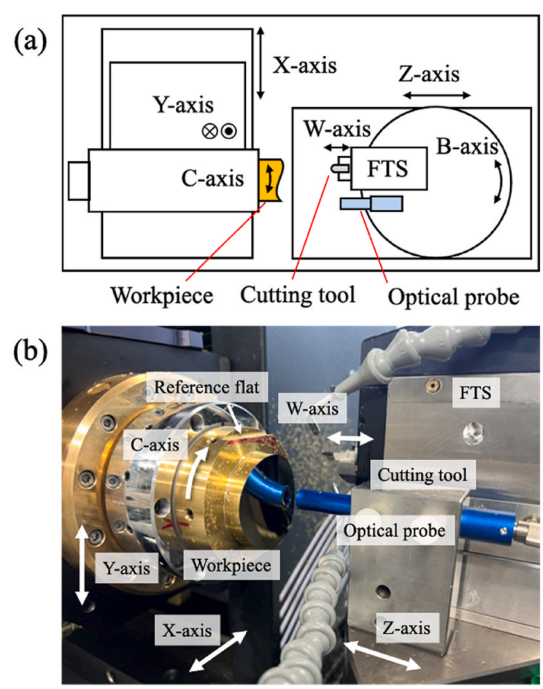

Fig. 6. (a) Machine setup layout, (b) machine setup picture of this experiment.

4. Experimental procedures

4.1. Experimental conditions

The design surface information is presented in Table 1. A concave cylindrical surface design was selected as the non-rotationally symmetric surface in this study. The ROC of the cylindrical surface was 110

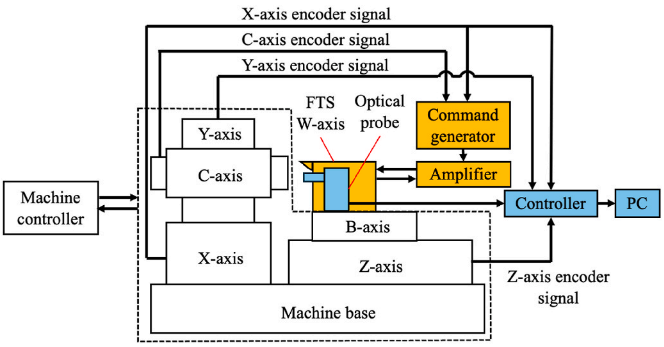

Fig. 7. System signal flow.

mm, and the workpiece diameter was 50 mm. From this design, the maximum sagitta height was 2.879 mm, and the maximum slope in the circumferential direction was 6.538°. A 360 brass was chosen as the workpiece material to minimize material-originated errors in the testing results. A single-crystal diamond tool with a 0.49 mm nose radius, 0° rake angle, and 10° clearance angle was used to avoid interference between the clearance face of the tool and the machined surfaces. The cutting conditions used in the experiments are summarized in Table 2.

4.2. On-machine clocking angle error measurement

The clocking angle error after machining was evaluated using a non-contact optical probe on the machine without removing the workpiece from the spindle. To assess the clocking angle error, the C-axis was aligned with the same reference used during machining, and the reference flat was aligned parallel to the X-axis. As illustrated in Fig. 9 (a), two profiles of the machined surface were scanned in the Y-axis direction using the optical probe. To eliminate the influence of tool-height errors on the cylindrical surface fabrication process, the scanning locations were selectively chosen on one side of the surface. Fig. 9(b) and (c) show the method of clocking angle error calculation. The clocking angle error $\Delta\varphi$ can be expressed as follows:

$$\Delta\varphi = \tan^{-1}\left(\frac{y_1 - y_2}{L}\right), \tag{7}$$

where y_1 is the profile peak location on the Y-axis at Location 1, y_2 is the profile peak location on the Y-axis at Location 2, and L is the distance between Locations 1 and 2. For the scanning locations, points 1 mm and 24 mm off-center were selected with a scanning length of 6 mm. The scanning speed was set to 50 mm/min, and the data sampling frequency was 32 Hz. Because the collected data were discrete, the captured data were fitted using a second-order polynomial to accurately determine the peak locations. The on-machine evaluation conditions are presented in Table 3.

4.3. FTS signal delay identification

The potential delay components should be decomposed and analyzed separately to identify the sources of time delay in the system. The analysis revealed three primary sources of delay. These are: i) servo delay, ii) communication delay, and iii) encoder signal-processing delay (Fig. 10). The total time delay in the system ΔT can be described by Equation (8):

$$\Delta T = \Delta T_1 + \Delta T_2 + \Delta T_3 \,. \tag{8}$$

First, servo delay due to the closed-feedback mechanism is typically observed as a system response, denoted as ΔT_1 in Fig. 10. This delay can be identified by acquiring the command and actual position data from the system's data acquisition function. The acquisition duration is 1.5 s, with a 20 kHz update rate, resulting in a 50 μs sampling period. To calculate the position feedback delay, these signals were logged while

Table 1
Design shape information.

Design shape	Value
Surface design	Concave cylinder
ROC (mm)	110
Diameter (mm)	50
Maximum sagitta (mm)	2.879
Maximum concentric slope (°)	6.538
Workpiece	
Material	360 Brass

Table 2
Cutting conditions.

Cutting conditions	Value
Cutting tool	
Tool material	Single-crystal diamond
Nose radius (mm)	0.49
Rake angle (°)	0
Clearance angle (°)	10
Cutting parameters	
Spindle rotation rate (rpm)	1000
Feed rate (mm/min)	Rough: 10 Finish: 2
Depth of cut (μm)	Rough: 5 Finish: 2
Coolant	Oil mist

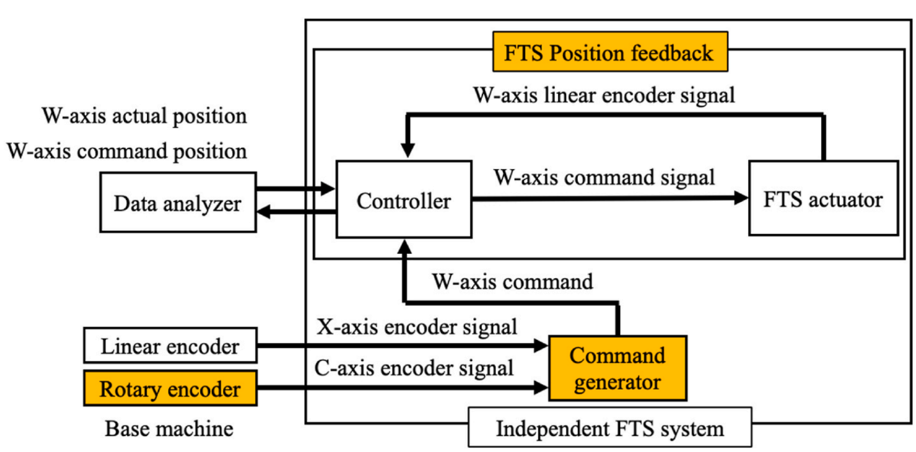

Fig. 8. Signal flow in detail inside FTS system.

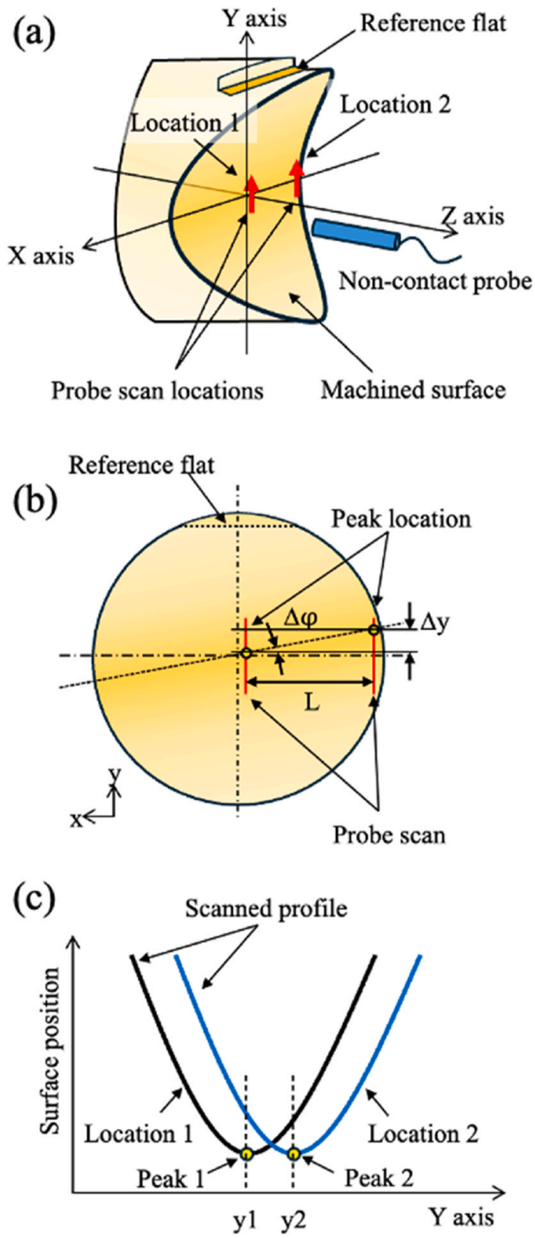

Fig. 9. On machine measurement procedure and data analysis method. (a) measurement location by non-contact probe, (b) clocking angle error calculation procedure method, (c) schematic of scanned profiles for peak detection.

Table 3
On-machine evaluation conditions.

On-machine evaluation conditions	Value
Non-contact surface probe	
Surface detection method	Chromatic confocal
Working distance (mm)	4.5
Measuring range (μm)	300
Axial resolution (nm)	2
Scanning parameters	
Scanning direction	Y-axis
Scanning speed (mm/min)	50
Sampling rate (Hz)	32

executing the part program on the machine without any machining processes. From this logged data, a segment of one rotation was extracted from an arbitrary point in the profile. The retrieved signals are illustrated in Fig. 11(a).

To enhance calculation resolution, cubic spline interpolation is applied with a factor of 200, generating intermediate points that reduce the data point interval from 50 μs to 0.25 μs. This point spacing defines the calculation's resolution. Fig. 11(b) demonstrates the methodology for quantifying time delays within a servo system using an error-minimization approach. It illustrates two primary curves: the commanded trajectory and the actual trajectory of the servo system over the sampling period. Due to the inherent time delay in the servo mechanism, a noticeable lag is observed between these two trajectories.

To analyze this delay, the actual profile is systematically shifted backward in time to determine the delay from the commanded trajectory. For each shift, the absolute difference in tool position between the commanded trajectory and the shifted actual trajectory is calculated and summed across all points. An error function E is defined to compute the sum of the absolute differences between the interpolated command position and the time-shifted actual position, expressed as follows:

$$E = \sum_{i=1}^{n} |W_c(t_i) - W_a(t_i - \Delta t)|, \tag{9}$$

where t_i represents the time indices of the interpolated data, and Δt indicates the time shift of the actual position data $W_a(t_i)$. The actual trajectory data $W_a(t_i)$ is shifted from 0 μs up to 500 μs in determined intervals. The optimal time shift Δt_{opt} that minimizes the error function E is identified using:

$$\Delta t_{opt} = argmin_{\Delta t}\, E,$$

$$subject\ to: 0\ \mu s \leq \Delta t \leq 500\ \mu s, \tag{10}$$

employing this fitting approach allows for the precise determination of time delays.

Second, regarding the W-axis command generation process, it is crucial to consider the time required to generate the W-axis command, denoted as ΔT_2 in Fig. 10. Given that the clocking cycle for updating the position is 20 kHz, the required processing time is 50 μs. Additionally, the latency—defined as the time needed to transmit data to the process component—is also set at 50 μs for accurate signal processing. Therefore, the total response time within the command-generating process consists of 50 μs for position calculation and 50 μs for transmission stability, resulting in an intentional delay of 100 μs within the system. This delay is designed to ensure precision and can be treated as a constant.

Third, an optical encoder system on the spindle detects the C-axis position information. The signal from the read-head detector is sent to the interpolator, which processes the signals before they are forwarded to the command generator in an independent FTS system. This interpolation also requires processing time, described as ΔT_3 in Fig. 10. However, because this delay occurs prior to reaching the independent FTS system, it cannot be captured by collecting signals from the FTS system. As a result, this quantity depends on the platform used. Consequently, the FTS system delay, calculated as $\Delta T_1 + \Delta T_2$, serves as the time compensation amount, while the time delay from the machine platform, ΔT_3, can be identified from the results of machining experiments.

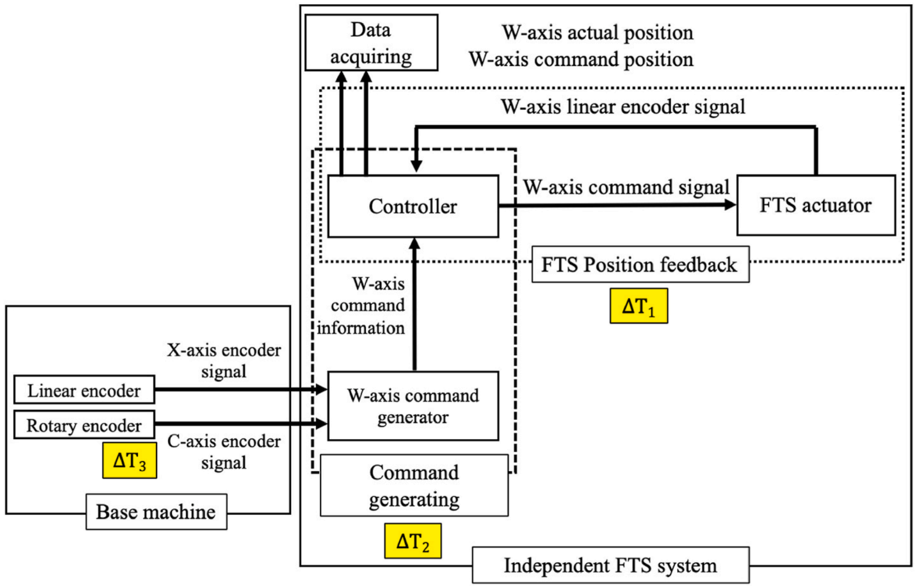

Fig. 10. Consideration of the location where the delay occurred.

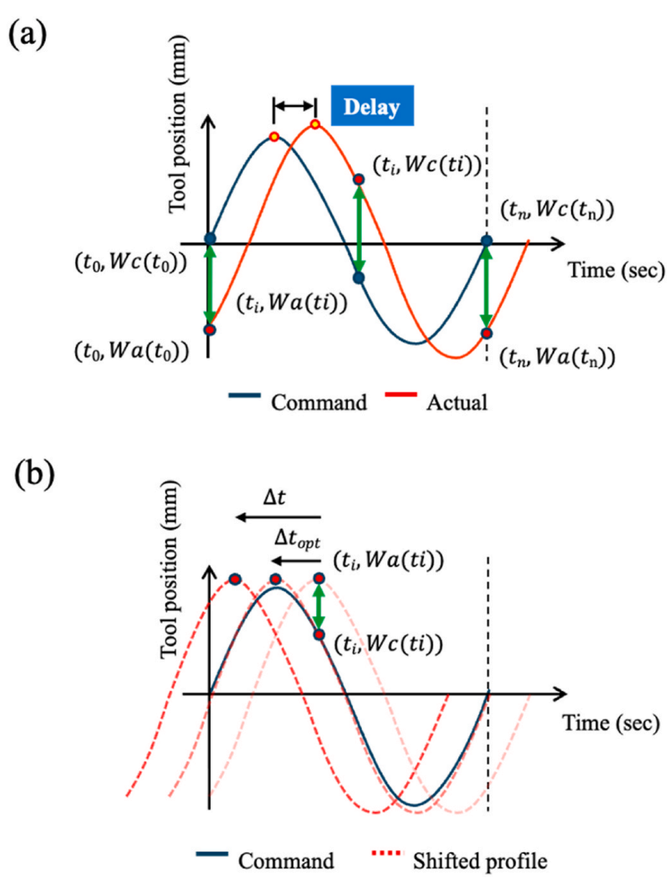

Fig. 11. Servo delay calculation method from acquired signals. (a) schematic of the captured command profile and actual profile, (b) schematic of the time delay calculation procedure.

4.4. Time delay compensation strategies

To compensate for this residual delay, Tanikawa et al. [26] utilized FTS angular misalignment calibration by calculating the time delay, which involved redefining the C-axis position in the programming. However, redefining the C-axis position for the compensation process necessitates re-evaluating the compensation amount in the part program whenever the cutting conditions, particularly the spindle speed, change. The use of direct compensation amounts over time is a more flexible approach to improve the time-delay compensation process. Therefore, a correction amount inserted directly over time into the system was proposed, as illustrated in Fig. 12.

First, the X- and C-encoder signals were converted into position information using their respective scale factors. The C-axis information was then entered into a speed detector, which calculated the spindle rotation speed in RPM. Using the spindle rotation speed and the time compensation input, the C-axis correction amount is determined using Equation (6) as the C-axis compensation position information. Consequently, this compensation amount is added to the original C-axis position, resulting in the updated C-axis position, $C + C_{comp}$. Thus, the updated C-axis position information is utilized as a function of the design information to generate the W-axis command.

4.5. Off-machine measurement and analysis

The off-machine measurements were conducted using a non-contact 3D laser autofocus system (NH-3SP Mitaka Koki Co., Ltd.) to collect surface information in 3D through raster scanning. The samples were then placed on the XY stage of a metrology platform. The reference flat of the workpiece was aligned parallel to the Y-axis, and raster scanning was performed along the X-axis, as illustrated in Fig. 13(a). The scanning speed was set at 100 mm/min, with data spacing in the X-axis direction of 0.1 mm and a stepover in the Y-axis direction of 2 mm.

To determine the clocking angle error from the raw measurement data, a data fitting process was applied to align the measured data with

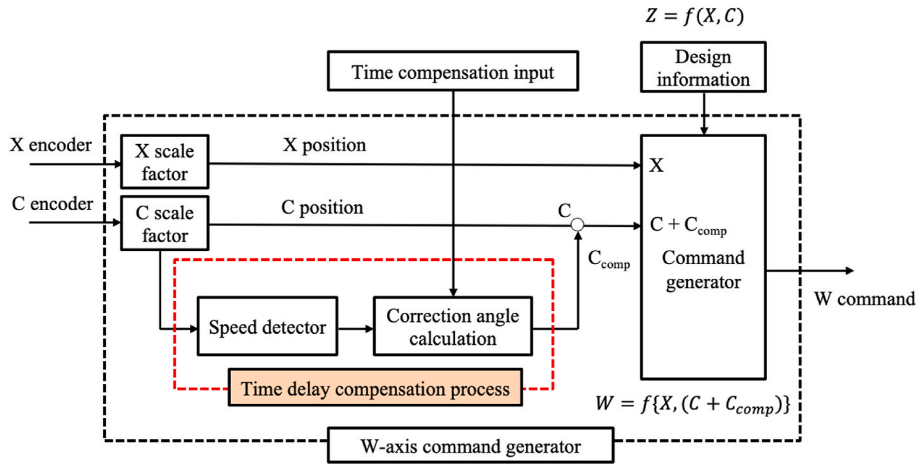

Fig. 12. Clocking angle error compensation process by adjusting time delay inside the system.

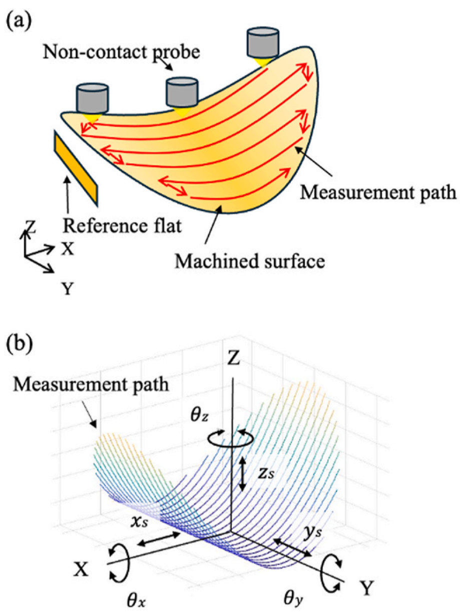

Fig. 13. Clocking angle error detection procedure by off-line measurement. (a) probe scan procedure by off-line non-contact probe, (b) translation and rotation directions for fitting process of measured data.

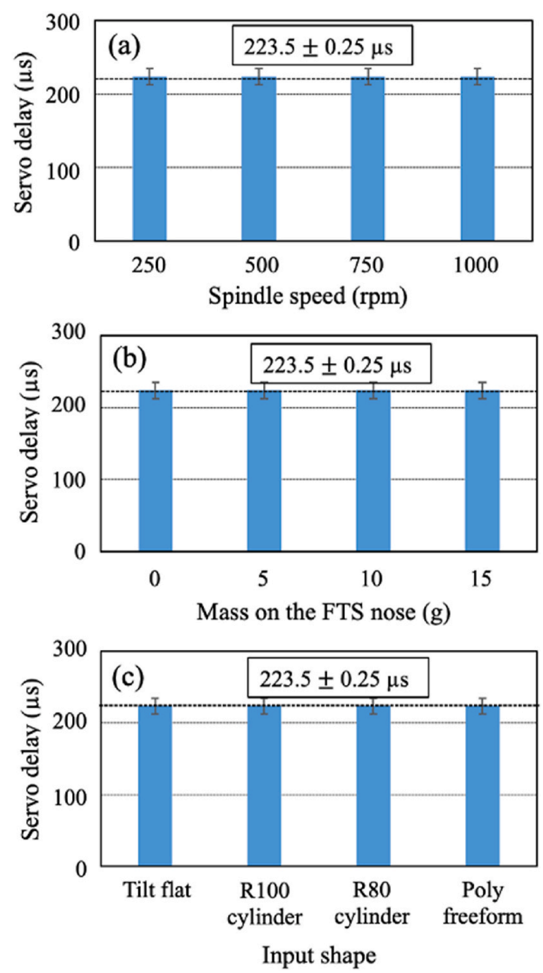

Fig. 14. Analysis result of servo delay in different conditions: (a) influence of spindle speed, (b) influence of mass on the FTS nose, (c) influence of input shapes into FTS.

an ideal surface, allowing for six degrees of freedom, as shown in Fig. 13 (b). In this study, the Levenberg-Marquardt fitting algorithm was utilized to minimize the distance between the measured raw data and the ideal surface using translation and rotation matrices. To assess the form accuracy of the surface, a cylindrical form removal process with a designed radius was applied following the translation and rotation fitting processes. The deviations of the peak-to-valley and RMS values after removing the designed cylinder from the aligned measurement data were used to evaluate form accuracy. For surface roughness evaluation, a Coherence Scanning Interferometry (CSI) optical profiler (NexView NX2, Zygo Corporation, USA) was employed to assess the machined surfaces with nanometer-level surface topography in three dimensions. The measurement area had a field of view of 350 μm^2 with a lateral resolution of 0.35 μm. A fourth-order polynomial form removal process was applied to analyze the surface roughness parameters.

5. Results and discussion

5.1. Servo delays under various operational conditions

The servo delays under different operational conditions were investigated using the method described in Section 4.3. The results are presented in Fig. 14(a) to 14(c). Fig. 14(a) illustrates the influence of spindle speed differences on the servo delay. Data were sampled 24 mm from the center while executing a program for a cylindrical surface with a ROC of 110 mm. The peak-to-valley value of the circumferential trajectory was 2.635 mm, forming two cycles in one rotation. The tested spindle speeds were 250, 500, 750, and 1000 rpm. At this location, the maximum velocities of the FTS actuator ranged from 0.070 m/s to 0.279 m/s, and the maximum accelerations ranged from 3.7 m/s^2 to 59.3 m/s^2 at 1000 rpm. Fig. 14(b) shows the influence of different mass conditions at the FTS nose on the servo delay. The tested conditions included no tool on the nose, 0 g, 5 g, 10 g, and 15 g. The trajectory shown in Fig. 14 (c) was used and tested at 1000 rpm. At this location, the maximum velocity of the FTS actuator was 0.738 m/s, and the maximum acceleration was 59.3 m/s^2.

Fig. 14(c) illustrates the influence of different input shapes on the servo delay. The investigated shapes included a tilt flat with a 5 mm height difference, cylindrical surfaces with ROC of 110 mm and 80 mm, and a polynomial freeform shape with multiple cycles of varying amplitudes. The cycles in one revolution ranged from one to four, at 24 mm from the center. At this location, maximum velocities ranged from 0.246 m/s to 0.738 m/s, and maximum accelerations ranged from 25.7 m/s^2 to 223.3 m/s^2 at 1000 rpm. According to these results in Fig. 14, the servo delay remained constant across each condition at 223.5 μs under the varied acceleration conditions in this experiment. The FTS counterbalance design effectively canceled out the inertial effects while operating within the performance capacity, particularly under an acceleration limit of 392.7 m/s^2 (40 G). The servo delay of the FTS actuator is treated as a constant amount in this experiment. In summary, the FTS system delay $\Delta T_1 + \Delta T_2$ was 223.5 μs + 100 μs = 323.5 μs ± 0.25 μs, which is a constant amount in this study.

5.2. Clocking angle error evaluation after time delay compensation

In the previous section, the FTS delay was calculated to be 323.5 μs under various operational conditions. Table 4 presents the results of the clocking angle error after applying a time compensation of 323.5 μs under the cutting conditions specified in Table 2. The average residual clocking angle error was found to be 0.0684° across eight machining tests. Converting this error to a time delay at a spindle speed of 1000 rpm corresponds to an average time delay of 11.40 μs. Regarding the reproducibility of the machining results, the angle error demonstrated a peak-to-valley value of 0.0015° and a standard deviation of 0.0005°. At a spindle speed of 1000 rpm, the reproducibility of the time delay measured 0.25 μs peak-to-valley and 0.075 μs standard deviation.

According to the results after compensating for the time delay in the FTS system, the residual time delay from the machine platform, denoted as ΔT_3, was found to be 11.40 μs with a standard deviation of 0.075 μs. This indicates that the signal processing and transfer times for the machine platform were 11.40 μs. Therefore, the total time delay of the system, including that of the machine platform, was 334.9 μs. The breakdown of the system time delay is as follows: i) 223.5 μs from the servo system, ii) 100 μs from the FTS command calculation, and iii) 11.4 μs from the machine platform. The residual clocking angle error results obtained after machining, compensating for the total delay, are listed in Table 5. The clocking angle error was reduced to 0.00014° with a corresponding residual time delay of 0.023 μs at 1000 rpm. The clocking angle error was effectively eliminated by identifying the time delay and compensating for it directly in the FTS system using the appropriate time values. These results confirm that the time delay outside the independent FTS system significantly impacts high-speed freeform machining. If the 11.4 μs time delay is not considered in FTS machining at a spindle speed of 1000 rpm, the estimated form error would be 6.8 μm peak-to-valley for the tested sample shape, which does not meet the appropriate form accuracy required for optical components. Therefore, accurately determining this amount from the machine platform is crucial for the total time-delay calculation process.

Table 4
Result of the clocking angle error after time delay compensation in FTS machining.

Number of tests	Measured angle (°)	Converted to time at 1000 rpm (μs)
1	0.0693	11.55
2	0.0687	11.45
3	0.0682	11.37
4	0.0685	11.42
5	0.0683	11.38
6	0.0678	11.30
7	0.0684	11.40
8	0.0681	11.35
Average	0.0684	11.40
Peak to valley	0.0015	0.25
Standard deviation	0.0005	0.075

Table 5
Comparison results of the clocking angle error before and after time compensation process.

Additional time correction (μs)	Clocking angle error (°)	Converted to time at 1000 rpm (μs)
323.5	0.0684	11.40
334.9	0.00014	0.023

In this experiment, the machine platform featured an optical encoder system on the spindle that detected the C-axis position. First, the read head detects the position of the C-axis from the gratings on the rotary encoder. Subsequently, the signal enters the interpolator to be smoothed or filtered for noise reduction before being sent to the FTS command generator. These processes require processing time [29,30] and cannot be detected by the independent FTS, resulting in a time delay described as ΔT_3 in Fig. 10. This indicates that a machining process is necessary to verify the total time delay, as the delay amount relies on the detection system, signal conversion, and interpolation used. Understanding the time delay from the machine platform and precisely calibrating the total delay are essential for effectively utilizing an independent FTS system for high-speed freeform fabrication.

5.3. Surface accuracy evaluation by off-line measurements

Fig. 15 illustrates the estimated form accuracy based on the obtained clocking angle error and the measurement results of form accuracy using an offline instrument. Fig. 15(a) and (b) present the offline measurement results before and after the additional time correction. Before the correction, the clocking angle error and form accuracy were 0.0700° and 6.6 μm PV, respectively. After the additional delay correction, these values improved to 0.0002° for the clocking angle error and 0.85 μm PV for form accuracy. By converting the measured clocking angle error to

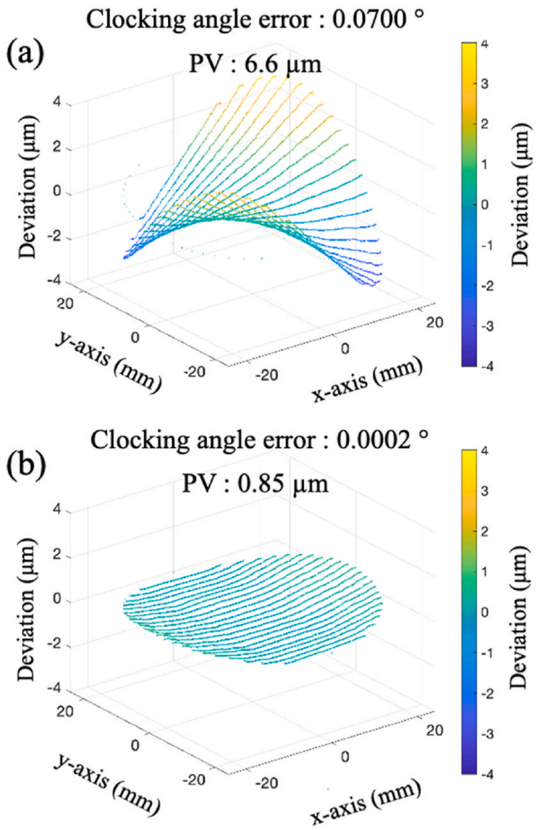

Fig. 15. Offline measurement comparison results before and after total time delay on FTS machining system. (a) before additional time delay compensation, (b) after additional time delay compensation.

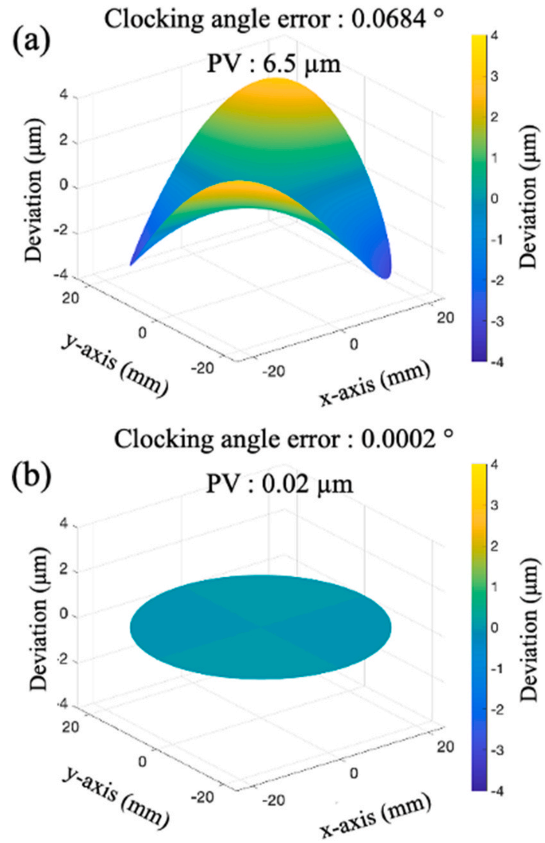

Fig. 16. Form error estimation by calculating the clocking angle error (a) before additional clocking angle compensation, (b) after additional clocking angle compensation.

the residual time delay using Equation (6), the residual time delay error was calculated to be 0.035 μs, indicating that the additional correction was effective, as confirmed by the offline metrology instrument. Regarding form accuracy, Fig. 16 shows the estimated form accuracy calculated with the clocking angle error obtained in Table 5 using Equation (4). Fig. 16(a) and (b) present the results before and after the additional compensation, respectively. The machining results indicate that the actual form accuracy was greater than the calculated values when comparing the results in Fig. 15(a) and (b). To address form accuracy after eliminating the time delay, the servo behavior must be considered; thus, further investigation into the elimination process is necessary.

The results of the surface roughness measurements are shown in Fig. 17(a). The surface roughness values of Sa and Sq in this experiment were 1.8 nm and 2.9 nm, respectively, indicating that the surface finish met the general requirements for the component. In comparison, the surface roughness of the brass flat, which had no FTS motion under the same cutting conditions as the cylinder machining, measured 1.8 nm Sa and 2.4 nm Sq, as shown in Fig. 17(b). This suggests that the surface roughness resulting from FTS cylinder machining was comparable and that correcting the time delay did not adversely affect the surface roughness.

Fig. 17(c) displays the surface outlook of the samples. Additionally, grain structures were observed in the surface roughness results, indicating that the material characteristics played a significant role in determining surface roughness. Therefore, it is possible that these surface roughness results represent the achievable limitations of this material.

5.4. Freeform surface machining with time delay compensation

The total time delay was calculated based on the previous discussion. A cylindrical freeform fabrication was conducted as an example, utilizing this time-delay identification within the FTS system. The shape information is presented in Table 6. The surface definition is described in Equations (11)–(13), with coefficients as follows: $Cx = -0.01$, $Ax_2 = 0.009646$, $Ax_4 = 1.57100 \times 10^{-9}$, $Ax_6 = 2.06489 \times 10^{-11}$, $Ax_8 = -7.25761 \times 10^{-12}$, $Ay_4 = -1.0983 \times 10^{-6}$. The maximum height difference in the shape was 2.25 mm. The same machining conditions for the cylindrical tests were applied, as detailed in Table 2. Fig. 18 (a) and (b) display the results of the clocking angle error and form accuracy measured by the offline instrument, while Fig. 18 (c) shows an overview of the machined freeform sample. By implementing a time compensation of 334.9 μs in the system, the residual clocking angle error was reduced to 0.0009°. When converting this at 1000 rpm, the calculated residual time delay was 0.15 μs. The estimated form accuracy at a clocking angle error of 0.0009° with the current cutting parameters is 0.063 μm PV

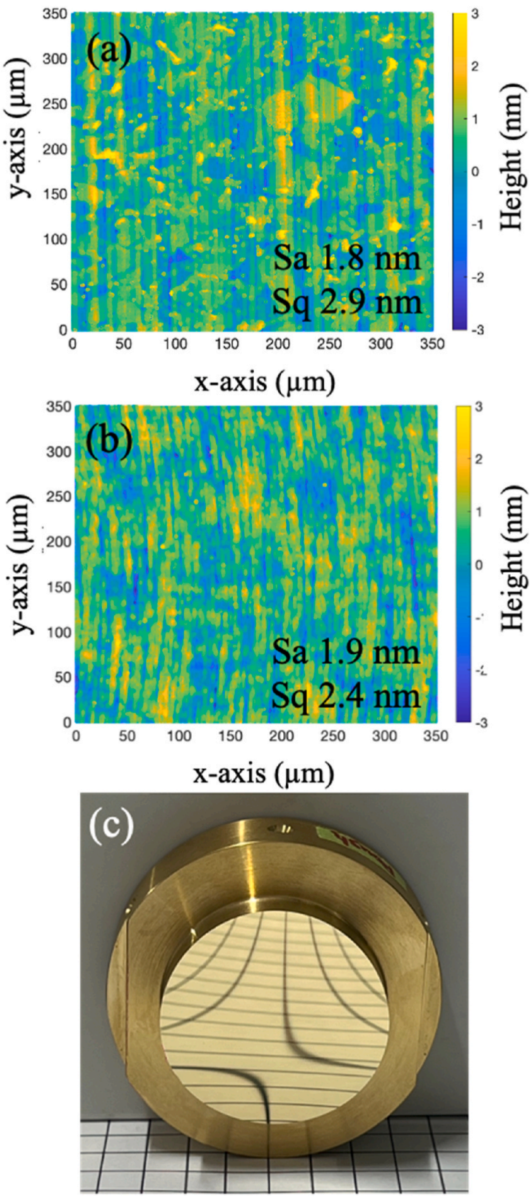

Fig. 17. (a) Surface roughness measurement result of the cylindrical surface, (b) surface roughness measurement result of the flat surface, (c) appearance of the machined cylindrical surface.

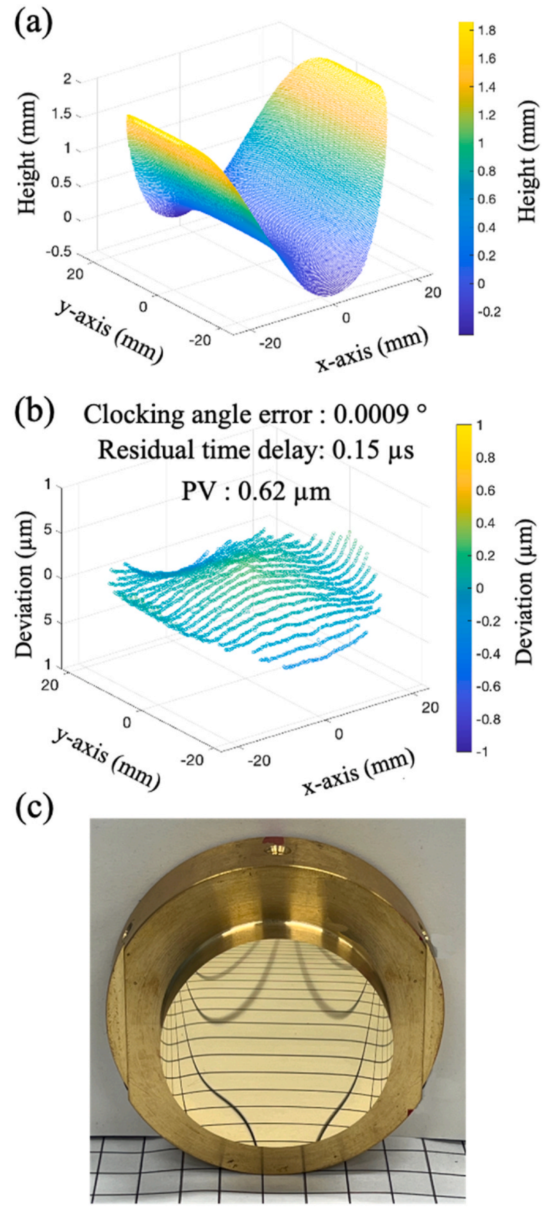

Fig. 18. (a) Cylindrical freeform shape, (b) off-line measurement result of the fabricated cylindrical freeform, (c) appearance of the cylindrical freeform surface.

Table 6
Cylindrical freeform design information.

Design shape	Value
Surface design	Concave cylindrical freeform
Diameter (mm)	50
Maximum sagitta (mm)	2.252
Maximum concentric slope (°)	4.673
Workpiece	
Material	360 Brass

from Equation (4). However, the achieved form accuracy was 0.62 μm PV. The peak and valley points of the form error were located at the inflection points of the cylindrical shape. Based on the measurement results, it can be inferred that servo overshooting occurred at the trajectory change point of the tool direction. Therefore, the observed form accuracy does not originate from the clocking angle error. This demonstration indicates that the proposed time-delay correction and calibration procedure was effective for various shape inputs.

$$Zx = \frac{Cx \cdot X^2}{1 + \sqrt{1 - (1 + kx) \cdot (Cx \cdot X)^2}} + Ax_2 \cdot X^2 + Ax_4 \cdot X^4 + Ax_6 \cdot X^6 + Ax_8 \cdot X^8, \tag{11}$$

$$Zy = \frac{Cy \cdot Y^2}{1 + \sqrt{1 - (1 + ky) \cdot (Cy \cdot Y)^2}} + Ay_2 \cdot Y^2 + Ay_4 \cdot Y^4 + Ay_6 \cdot Y^6 + Ay_8 \cdot Y^8, \tag{12}$$

$$Z = Zx + Zy. \tag{13}$$

6. Conclusion

The time delay in independently controlled fast tool servo (FTS) system significantly affected the clocking angle error. This study evaluated the influence of the clocking angle error on freeform diamond turning using FTS and proposed a compensation method for the time delay. Non-rotationally symmetric surfaces, such as cylindrical and freeform surfaces, were machined to verify the time-delay compensation process. The main conclusions are as follows.

a) In the high-speed FTS diamond-turning process, the clocking angle error is a crucial factor in form error control. The peak-to-valley form error was analyzed using the local slope in the circumferential direction of the given surface and the clocking angle error. Based on this analysis, the local displacement error is described as the product of the local slope in the circumferential direction, the clocking angle error, and the distance from the rotation center to the point of interest. Therefore, the delay in the high-speed FTS machining of freeform surfaces, such as at a spindle speed of 1000 rpm, significantly affects the form error.
b) The time delay of the FTS system was found to be composed of three significant components: the first was the time delay from the servo control, the second was the designed processing time to generate the W-axis command, and the third was the C-axis encoder signal processing time within the base machine platform. According to the time delay results, it was realized that the servo control delay was the most dominant factor. In this experiment, the delays were identified as 223.5 μs for servo control, 100 μs for processing time, and 11.4 μs for C-axis encoder signal processing.
c) The total time delay of the proposed FTS system was determined to be 334.9 μs. By compensating for this delay directly in the system over time, the residual clocking angle error was reduced to 0.00014° (evaluated by on-machine measurement) and 0.00020° (by off-line metrology), respectively, with form accuracy achieved at 0.85 μm peak-to-valley.
d) The C-axis encoder signal processing time delay (11.4 μs) was found to be more significant than the required time delay control amount and could not be recognized within the FTS system. Therefore, the calibration process for the time delay, including that of the machine platform, is essential.
e) A cylindrical freeform shape was machined using the calibrated time-compensation amount, resulting in a residual clocking angle error of 0.0009° (evaluated by off-line metrology) and a residual time delay of 0.15 μs at 1000 rpm after compensation. This indicates that the proposed time delay identification and calibration procedure can effectively be used for machining different freeform shapes using the FTS system.

This study demonstrated the importance of identifying system time delays in high-speed freeform diamond-turning using FTS. The methodologies for time-delay identification and compensation were established, contributing to the advanced manufacturing of optical components and enhancing productivity. As a residual form error was still observed after time-delay compensation, the authors plan to focus on further improving form accuracy by considering additional factors beyond the clocking angle error as a future task.

CRediT authorship contribution statement

Takeshi Hashimoto: Writing – original draft, Visualization, Validation, Methodology, Investigation, Formal analysis, Data curation, Conceptualization. **Jiwang Yan:** Writing – review & editing, Supervision, Resources, Project administration, Methodology, Conceptualization.

Declaration of competing interest

The authors declare that they have no known competing financial interests or personal relationships that could have appeared to influence the work reported in this paper.

Acknowledgement

The authors thank AMETEK Precitech Inc. and Zygo Corporation for their technical support with the experimental equipment.

References

[1] Xie Y, Mao X, Li J, Wang F, Wang P, Gao R, Li X, Ren S, Xu Z, Dong R. Optical design and fabrication of an all-aluminum unobscured two-mirror freeform imaging telescope. Appl Opt 2020;59(3):833–40. https://doi.org/10.1364/AO.379324.
[2] Rao BV, Kiran M, Ramaswamy V, Sriram KV. Convex optical freeforms using fringe Zernike overlay approach for two-mirror and three-mirror telescopes for space applications. Opt Commun 2023;541:129533. https://doi.org/10.1016/j.optcom.2023.129533.
[3] Liu J, Lombardo S, Muslimov E, Chebbo M, Hugot E. Innovative optical design combining freeform optics and curved-freeform sensors. Advances in optical and mechanical technologies for telescopes and instrumentation V. Proc SPIE 2022; 2022:12188O. https://doi.org/10.1117/12.2629193.
[4] Li Z, Fang F, Chen J, Zhang X. Machining approach of freeform optics on infrared materials via ultra-precision turning. Opt Express 2017;25(3):2051–62. https://doi.org/10.1364/OE.25.002051.
[5] Maimone A, Wang J. Holographic optics for thin and lightweight virtual reality. ACM Trans Graph 2020;39(4):67:1–67:14. https://doi.org/10.1145/3386569.3392416.
[6] Kress BC, Pace M. Holographic optics in planar optical systems for next generation small form factor mixed reality headsets. Light Adv Manuf 2022;3(4):771–81. https://doi.org/10.37188/lam.2022.042.
[7] Cakmakci O, Qin Y, Bosel P, Wetzstein G. Holographic pancake optics for thin and lightweight optical see-through augmented reality. Opt Express 2021;29(22): 35206–15. https://doi.org/10.1364/OE.439585.
[8] Narasimhan BA. Ultra-compact pancake optics based on ThinEyes® super-resolution technology for virtual reality headsets. Proc SPIE 2018;10676. https://doi.org/10.1117/12.2315688. Digital Optics for Immersive Displays.
[9] Thompson KP, Rolland JP. Freeform optical surfaces: a revolution in imaging optical design. Opt Photon News 2012;23(6):30–5.
[10] Wei L, Li Y, Jing J, Feng L, Zhou J. Design and fabrication of a compact off-axis see-through head-mounted display using a freeform surface. Opt Express 2018;26(7): 8550–65. https://doi.org/10.1364/OE.26.008550.
[11] Ye Z, Yan J, Jiang T, Chen S, Xu Z, Feng H, Li Q, Chen Y. Design of an optimized Alvarez lens based on the fifth-order polynomial combination. Appl Opt 2023;62 (34):9072–81. https://doi.org/10.1364/AO.501295.
[12] Babington J. Alvarez lenses: theory and applications. Optical design and engineering VI. Proc SPIE; 2015. https://doi.org/10.1117/12.2193114. 9626.
[13] Niu K, Tian C. Zernike polynomials and their applications. J Opt 2022;24(12): 123001. https://doi.org/10.1088/2040-8986/ac9e08.
[14] Mahajan VN. Zernike circle polynomials and optical aberrations of systems with circular pupils. Appl Opt 1994;33(34):8121–4. https://doi.org/10.1364/AO.33.008121.
[15] Kyrish M, Cardenas N, Fraelich M, Lechuga O, Claytor R, Claytor N. Fabricated freeform optics. Imaging and Applied Optics 2015. https://doi.org/10.1364/AOMS.2015.JT5A.5.
[16] Kumar S, Tong Z, Jiang X. Advances in the design and manufacturing of novel freeform optics. Int J Extrem Manuf 2022;4(3):032004. https://doi.org/10.1088/2631-7990/ac7617.
[17] Fang FZ, Zhang XD, Weckenmann A, Zhang GX, Evans C. Manufacturing and measurement of freeform optics. CIRP Ann - Manuf Technol 2013;62(2):823–46. https://doi.org/10.1016/j.cirp.2013.05.003.
[18] Mishra V, Burada DR, Pant KK, Karar V, Jha S, Khan GS. Form error compensation in the slow tool servo machining of freeform optics. Int J Adv Manuf Technol 2019; 105(1–4):1623–35. https://doi.org/10.1007/s00170-019-04359-w.

[19] Chen CC, Huang CY, Peng WJ, Cheng YC, Yu ZR, Hsu WY. Freeform surface machining error compensation method for ultra-precision slow tool servo diamond turning. Optical manufacturing and testing X. Proc SPIE; 2013, 88380Y. https://doi.org/10.1117/12.2022981. 8838.

[20] Nagayama K, Yan J. Deterministic error compensation for slow tool servo-driven diamond turning of freeform surface with nanometric form accuracy. J Manuf Process 2021;64:45–57. https://doi.org/10.1016/j.jmapro.2021.01.015.

[21] AMETEK Precitech Inc. Fast tool servo. https://www.precitech.com/product/accessoriesoverview/fasttoolservo/. [Accessed 1 August 2024].

[22] Liang J, Dai Y, Guan C, Tie G, Xue S, Du C. Fast Axis servo diamond turning of complex surfaces. J Phys Conf Ser 2021;1789(1):012003. https://doi.org/10.1088/1742-6596/1789/1/012003.

[23] Sato Y, Yan J. Tool path generation and optimization for freeform surface diamond turning based on an independently controlled fast tool servo. Int J Extrem Manuf 2022;4(2). https://doi.org/10.1088/2631-7990/ac5f12.

[24] Tian F, Yin Z, Li S. Fast tool servo diamond turning of optical freeform surfaces for rear-view mirrors. Int J Adv Manuf Technol 2015;80(9–12):1759–65. https://doi.org/10.1007/s00170-015-7152-9.

[25] Roblee JW. Characteristics of systems that rapidly diamond turn non-rotationally symmetric surfaces. Proc JSPE Semestrial Meeting 2005;2005S(I80):489. https://doi.org/10.11522/pscjspe.2005S.0.489.0.

[26] Tanikawa S, Sato Y, Yan J. A novel calibration method for angular misalignment in independently controlled fast tool servo-based diamond turning. Precis Eng 2023;83:216–27. https://doi.org/10.1016/j.precisioneng.2023.06.010.

[27] Na J, Ren X, Costa-Castelló R, Guo Y. Repetitive control of servo systems with time delays. Robot Autonom Syst 2014;62(3):319–29. https://doi.org/10.1016/j.robot.2013.09.010.

[28] Watanabe K, Yamada K. Repetitive control of time-delay systems. Proc 29th IEEE Conf Decision Control 1990;3:1685–90. https://doi.org/10.1109/CDC.1990.203908. Honolulu, HI, USA.

[29] HEIDENHEIN. Technical information. https://www.heidenhain.us/addl-materials/enews/stories_1012/EnDat.pdf/. [Accessed 1 August 2024].

[30] Renishaw. Optical encoders frequently asked questions. https://www.renishaw.com/en/optical-encoders-frequently-asked-questions–34674/. [Accessed 1 August 2024].